Polarized Radiative Transfer for Zeeman-Split Oxygen Lines in the EOS MLS Forward Model

Michael J. Schwartz, William G. Read, W. Van Snyder

***Abstract*— The EOS MLS clear-sky unpolarized forward model [1] is supplemented by algorithms for the modeling of polarized emission from Zeeman-split spectral lines. This model accounts for polarization-dependent emission and correlation between polarizations with complex, 2x2 intensity and absorption matrices.**

***Index Terms*— Zeeman, EOS Aura, MLS, Forward Model**

I. Introduction

The EOS Microwave Limb Sounder (MLS) instrument [2], one of four instruments on the Aura spacecraft launched on 15 July 2004, measures thermal millimeter-wave emission from the Earth's limb. Atmospheric composition and temperature from roughly 8 km to 96 km are inferred from these measurements. At the highest-altitude pointings of the MLS limb scan, the primary source of temperature information is the line center of the 118-GHz oxygen line, which is opaque up into the lower thermosphere when viewed through the limb. This line is Zeeman-split into three components by the coupling of oxygen's electronic spin with the geomagnetic field. Doppler-broadened Zeeman components in the mesosphere and lower thermosphere are resolved by two MLS 100-kHz-resolution digital autocorrelator spectrometers (DACS) with orthogonal linear polarizations.

Absorption and emission in a given direction by the resolved Zeeman components depends upon the relative orientations of the geomagnetic field, the direction of radiation propagation and its polarization. The magnetic susceptibility has off-diagonal elements that mix polarizations as the wave propagates, so that the equations of radiative transfer for orthogonal polarizations are coupled. Lenoir [3][4] developed methods of doing radiative transfer calculations with 2x2 coherence matrix tensors, and applied this theory to the case of Zeeman-split microwave oxygen lines. Further relevant work has been done by Rosenkranz and Staelin [5] and Stogryn [6].

II. Spectroscopy

The electronic ground state of diatomic oxygen (O_2) is a triplet state (electronic spin quantum number $s = 1$); the spin has an associated magnetic dipole moment, $\mu = g_s s\hbar$, where $g_s = -2.0023\,\mu_{\text{B}}/\hbar$ is the electron gyro-magnetic ratio and μ_{B} is the Bohr magneton. Oxygen's microwave spectrum consists of magnetic dipole transitions that reorient this spin relative to the molecule's end-over-end rotation (quantum number N).

M.J. Schwartz, W.G. Read and W.V. Snyder are with the Jet Propulsion Laboratory, 4800 Oak Grove Dr. Pasadena, CA 91109

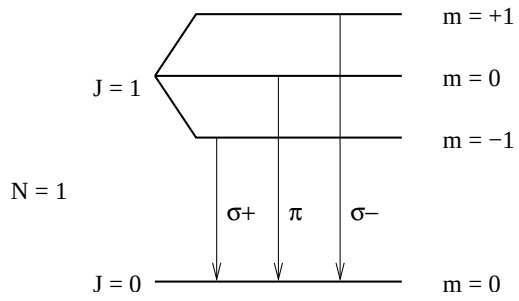

Fig. 1. The 1_- line has three Zeeman components. This figure is not to scale as all three transitions are approximately 118751 MHz, while the Zeeman splitting in typical geomagnetic fields is only of order 1 MHz.

The 118-GHz oxygen line is a transition between two states that are both approximately $N = 1$. (N is actually not a "good" quantum number as stationary states have small admixtures of different N's, but the predominant value is a useful label.) The upper state of the 118-GHz line has total angular momentum $J = 1$, and the lower has $J = 0$. Transitions are labeled N_+ when $J{=}N \longrightarrow J{=}N{+}1$ and N_- when $J{=}N \rightarrow J{=}N{-}1$, so the 118-GHz line is 1_-. The upper state has three possible projections (quantum number m) of J on the direction of an externally applied magnetic field, and the associated time-averaged projection of μ on the external field results in Zeeman splitting of the line, as shown schematically in Fig. 1. The magnitude of the energy shift of a given state is $mg\mu_{\text{B}}\mathcal{B}_{\text{geo}}$, where g is from the JPL line database [7] and $\mathcal{B}_{\text{geo}}$ is the magnitude of the geomagnetic field, $\boldsymbol{\mathcal{B}}_{\text{geo}}$. For the upper state of the 1_- line, $g = 1.0011$, the same value that one obtains from a simple, Hund's case b vector model [8]. The splitting of the upper state is ± 1.4012 MHz per gauss of applied field, less than ± 1 MHz in typical geomagnetic fields.

III. Tensor magnetic susceptibility

Dispersion and absorption by magnetic dipole lines are governed by the real and imaginary parts of the magnetic susceptibility, χ. In the scalar case, the wave equation for H,

$$\frac{\partial^2 H}{\partial z^2} H(\omega, z) + k_0^2 [1 + \chi(\omega)] H = 0 \tag{1}$$

has independent solutions for each transverse mode

$$H = H_0 e^{\imath (k_0 (1 + \frac{\chi(\omega)}{2}) z - \omega t)}. \tag{2}$$

Resolved Zeeman components have a 3x3, rank-2 tensor magnetic susceptibility, $\boldsymbol{\chi}^{(3)}$,

$$\boldsymbol{B} = (1 + 4\pi\boldsymbol{\chi}^{(\mathbf{3})})\boldsymbol{H}\,, \tag{3}$$

that couples the two radiation modes.

Magnetic dipole transitions can change the magnetic quantum number, m, by $+1$, 0 or -1; these types of transitions are called σ_+, π, and σ_- respectively. The three eigenvectors of the tensor magnetic susceptibility, $\boldsymbol{\chi}^{(\mathbf{3})}$, link three radiation polarizations to these three allowed values of Δm. The factoring of a common angular dependence for all lines in each of σ_+, π, and σ_- is a manifestation of the Wigner-Eckart theorem [3].

Linearly-polarized radiation with its $\hat{\boldsymbol{H}}_{\rm RF}$ vector along the imposed field direction couples only to π transitions while right and left-circular polarizations propagating along the external field couple only to σ_+ and σ_- transitions, respectively. Knowing these eigen polarizations, we can write the angular dependence of $\boldsymbol{\chi}^{(\mathbf{3})}$ in a right-hand, Cartesian basis where the third dimension is the direction of the externally applied field.

$$\boldsymbol{\chi}^{(\mathbf{3})} = \begin{bmatrix} (\chi_+ + \chi_-)/2 & -\imath(\chi_+ - \chi_-)/2 & 0 \\ \imath(\chi_+ - \chi_-)/2 & (\chi_+ + \chi_-)/2 & 0 \\ 0 & 0 & \chi_0 \end{bmatrix}. \tag{4}$$

Here, χ_+, χ_- andχ_0 are the eigenvalues of $\boldsymbol{\chi}^{(\mathbf{3})}$.

Now we rotate $\boldsymbol{\chi}^{(\mathbf{3})}$ (a rank-2 tensor rotates with a pair of 3x3 rotation matrices) so that $\hat{z}$ is the direction of propagation of a plane wave and $\hat{x}$ and $\hat{y}$ are its linear (defined by $\hat{\boldsymbol{E}}_{\rm RF}$) polarization basis. The rotation angles, θ and ϕ, are defined in Fig. 2.

If the magnetic-dipole coupling is weak ($\chi_{ij} \ll 1$) waves propagating through the medium will be approximately transverse [3] and the $\hat{z}$ dimension may be dropped from the radiation field equations. As $\hat{\boldsymbol{H}}_{\rm RF}$ is confined to the $x-y$ plane, there is no need for z-components of $\boldsymbol{\chi}^{(\mathbf{3})}$ and we project it into the two transverse dimensions.

$$\boldsymbol{\chi} = \chi_+\boldsymbol{\rho_+} + \chi_0\boldsymbol{\rho_0} + \chi_-\boldsymbol{\rho_-}\,, \tag{5}$$

where

$$\boldsymbol{\rho}_\pm = \boldsymbol{R}_\phi \begin{bmatrix} 1 & \mp\imath\cos\theta \\ \pm\imath\cos\theta & cos^2\theta \end{bmatrix} \boldsymbol{R}_\phi^\dagger\,, \tag{6}$$

$$\boldsymbol{\rho}_0 = \boldsymbol{R}_\phi \begin{bmatrix} 0 & 0 \\ 0 & \sin^2\theta \end{bmatrix} \boldsymbol{R}_\phi^\dagger\,, \tag{7}$$

and

$$\boldsymbol{R}_\phi = \begin{bmatrix} \cos\phi & \sin\phi \\ -\sin\phi & \cos\phi \end{bmatrix}. \tag{8}$$

The coefficients χ_+, χ_- andχ_0 are complex scalars, sums of the lineshapes of all lines of a given Δm, while the $\boldsymbol{\rho}$ contain the matrix nature of the polarized radiative transfer equation. A more detailed and pedagogical presentation of the origins of the polarized radiative transfer equations may be found in [9].

IV. Polarized Radiative Transfer

The polarized radiative transfer expressions give the evolution of an intensity matrix, $\boldsymbol{I}$, as radiation propagates through the atmosphere. The form of $\boldsymbol{I}$ that we use in this paper is Lenoir's definition [3], and has elements,

$$\boldsymbol{I} = \begin{bmatrix} I_{\parallel} & I_{|} + \imath I_{\circ} \\ I_{|} - \imath I_{\circ} & I_{\perp} \end{bmatrix}, \tag{9}$$

where $I_{\parallel}$ and $I_{\perp}$ are radiated power (scalar brightness temperatures) in linear polarizations respectively parallel and perpendicular to some reference direction, such as the linear polarization direction of an antenna. $I_{\circ}$ and $I_{|}$ are their circular and linear coherences.

We adopt the limb-path layer indexing scheme of the unpolarized algorithm [1], in which the first layer boundary is the top of the atmosphere closest to the observer, the tangent point is doubly-labeled t and $2N - t + 1$, and the top of the atmosphere beyond the tangent point is $2N$. This indexing is shown in Fig. 3. Double-indexing of the tangent point facilitates insertion of a surface term when rays intersect the earth's surface.

An expression for polarized radiation emerging from the top of the atmosphere closest to the observer may be cast in a differential-temperature form identical to that used in the unpolarized model [1],

$$\boldsymbol{I} = \sum_{i=1}^{t} \boldsymbol{\mathcal{T}}_i\,\Delta B_i + \sum_{i=2N-t+1}^{2N} \boldsymbol{\mathcal{T}}_i\,\Delta B_i\,. \tag{10}$$

The differential temperature, ΔB_i, is a function of B_i, the scalar Planck source function for thermal radiation in

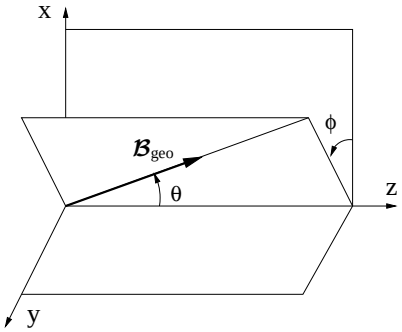

Fig. 2. Angles θ and ϕ defi ne the orientation or the geomagnetic fi eld $\boldsymbol{\mathcal{B}}_{\rm geo}$ relative to the x and y linear polarization basis for a wave propagating in the z direction.

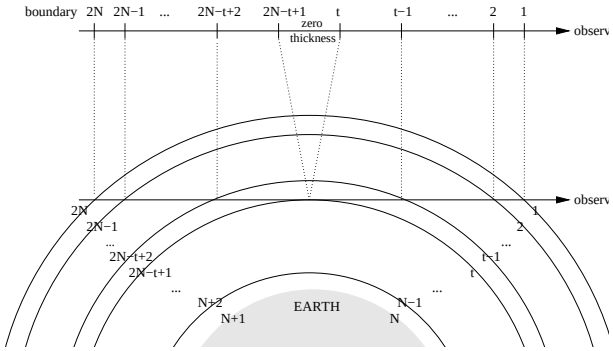

Fig. 3. This indexing scheme labels layer boundaries along a limb path.

equilibrium at layer-boundary temperature, T_i,

$$B_i = \frac{h\nu}{k(\exp\{\frac{h\nu}{kT_i}\}-1)}\,. \tag{11}$$
$$\Delta B_i = \frac{B_{i+1}-B_{i-1}}{2}\,,$$

with special cases

$$\Delta B_1 = \frac{B_1+B_2}{2}\,,$$
$$\Delta B_{2N} = B(T_{cosmic}) - \frac{B_{2N}+B_{2N-1}}{2}\,,$$

and to handle the jump at the tangent point,

$$\Delta B_t = \frac{B_t - B_{t-1}}{2}\,,$$
$$\Delta B_{2N-t+1} = \frac{B_{2N-t+2}-B_t}{2}\,. \tag{12}$$

Radiances are in Kelvin, so the leading factor in (11) is $h\nu/k$ rather than $2h\nu^3/c^2$.

$\boldsymbol{\mathcal{T}}_i$ is the *power* transmittance tensor from the i*th* layer boundary to the top of the atmosphere. It the product of a pair of *field* transmittances, $\boldsymbol{P}_i$,

$$\boldsymbol{\mathcal{T}}_i = \boldsymbol{P}_i\,\boldsymbol{P}_i^\dagger\,. \tag{13}$$

$\boldsymbol{P}_i$ is constructed of *field* layer transmittances, $\boldsymbol{E}_i$, using the recursion relation,

$$\boldsymbol{P}_1 = \mathbf{1}\,,$$
$$\boldsymbol{P}_i = \boldsymbol{P}_{i-1}\,\boldsymbol{E}_i\,,$$

with a special case for the transmittance between the two instances of the tangent point,

$$\boldsymbol{P}_{2N-t+1} = \boldsymbol{P}_t\,\Upsilon_f\,. \tag{14}$$

For rays that intersect the geoid, Υ_f is the *field* surface reflectivity matrix, the square root of the *power* surface reflectivity of [1]. Otherwise, Υ_f is unity. *Field* layer transmittances $\boldsymbol{E_i}$ are defined in terms of *field* incremental opacities,$\boldsymbol{\Delta\delta}^k_{i\to i-1}$

$$\boldsymbol{E}_1 = \mathbf{1}\,,$$
$$\boldsymbol{E}_i = \exp\left\{-\sum_k^{\text{species}} \boldsymbol{\Delta\delta}^k_{i\to i-1}\right\}\,. \tag{15}$$

$\boldsymbol{\mathcal{T}}_i$ is manifestly Hermitian, and may be thought of as a sandwich of $\boldsymbol{E}_i$ and $\boldsymbol{E}_i^\dagger$ matrices with the earliest times (largest indices) in the middle. Order is important as the $\boldsymbol{E}_i$ matrices generally do not commute with one another.

The incremental opacity integral due to polarized O_2 lines is

$$\begin{aligned}\boldsymbol{\Delta\delta}^{\mathrm{O_2}}_{i\to i-1} &= \int_{s_i}^{s_{i-1}} \frac{\imath k_0}{2}\boldsymbol{\chi}\,\mathrm{d}s \\ &= \frac{\Delta s^{\text{refr}}_{i\to i-1}}{\Delta s_{i\to i-1}} \sum_{\Delta m=-1}^{+1} \boldsymbol{\rho}_{\Delta m}(\theta,\phi)\,\xi_{m,\Delta m} \\ &\quad\times \int_{\zeta_i}^{\zeta_{i-1}} \mathsf{f}^{\mathrm{O_2}}(\zeta)\,\beta^{\mathrm{O_2}}_{\Delta m}(\zeta),\nu)\,\frac{\mathrm{d}s}{\mathrm{d}h}\frac{\mathrm{d}h}{\mathrm{d}\zeta}\,\mathrm{d}\zeta\,,\end{aligned} \tag{16}$$

TABLE I
ZEEMAN FRACTIONAL INTENSITIES, $\xi(m,\Delta m)$

	Δm	N_+	N_-	1_-
σ_+	+1	$\frac{3(N+m+1)(N+m+2)}{4(N+1)(2N+1)(2N+3)}$	$\frac{3(N-m)(N-m-1)}{4N(2N+1)(2N-1)}$	$\frac{1}{2}$
π	0	$\frac{3[(N+1)^2-m^2]}{(N+1)(2N+1)(2N+3)}$	$\frac{3(N^2-m^2)}{N(2n+1)(2N-1)}$	1
σ_-	-1	$\frac{3(N-m+1)(N-m+2)}{4(N+1)(2N+1)(2N+3)}$	$\frac{3(N+m)(N+m-1)}{4N(2N+1)(2N-1)}$	$\frac{1}{2}$

where $\xi_{m,\Delta m}$ is from Table I, $\mathsf{f}^{\mathrm{O_2}}(\zeta,\phi(\zeta))$ is the O_2 mixing ratio on its species representation basis. Here, we are chain-ruling from pathlength s to height h to negative-log-pressure, ζ. Expressions for $\frac{\mathrm{d}s}{\mathrm{d}h}$ and $\frac{\mathrm{d}h}{\mathrm{d}\zeta}$ are as in [1, Eqn. 48]

As is discussed in Section III, the $\boldsymbol{\rho}$ terms are purely functions of the orientation of the propagation direction with respect to the geomagnetic field. They contain all of the angular dependence and all of the 2x2 tensor-nature of the expression. These terms are common for all lines with the same ΔM, though in the case of the 118-GHz line, there is only one Zeeman component for each ΔM. All of the other terms in (16) are scalars.

For species that are isotropic absorbers, (*i.e.* $k \neq \mathrm{O_2}$), the field incremental opacity matrix is half of the scalar power incremental opacity of [1] times the identity matrix.

$$\boldsymbol{\Delta\delta}^k_{i\to i-1} = \frac{1}{2}\Delta\delta^k_{i\to i-1}\,\mathbf{1}\,. \tag{17}$$

Polarized power transmittance, $\boldsymbol{\mathcal{T}}$, is formed from products of pairs of *field* transmittances, which depend exponentially upon the cross-sections. The two half-power cross-sections add so that each of the diagonal elements correctly gives the scalar result for unpolarized radiation. We can restrict the lineshapes for unpolarized species to their real (absorptive) parts; when all of the $\boldsymbol{\rho}$ matrices are multiplied by the same complex coefficient, they add to a multiple of the identity matrix and the imaginary parts of the coefficients cancel in the construction of $\boldsymbol{\mathcal{T}}$.

A. Cross-Section $\boldsymbol{\beta}$

For oxygen Zeeman components, *field* cross-sections, β, have the same form as the *power* cross-sections of the scalar model, but in addition to the factor of one half, they require complex lineshapes, and line center positions are Zeeman shifted by the geomagnetic field. Following the notation of [**?**], the field cross-section β^k is

$$\beta^k = \frac{1}{2}\,\mathcal{R}^k\,\sqrt{\frac{\ln 2}{\pi}}\frac{10^{-13}}{kTw_d^k}\,P\sum_j 10^{S_j^k}\mathcal{F}\left(x_j^k,y_j^k\right)\,, \tag{18}$$

where

$$\begin{aligned}\mathcal{S}_j &= \mathcal{I}_j\left(T_0\right) + \log\left[\frac{Q^k(T_0)}{Q^k(T)}\right] + \frac{hc}{k}E''^k_j\left(\frac{1}{T_0}-\frac{1}{T}\right) \\ &+ \log\left[\tanh\left(\frac{h\nu}{2kT}\right)\right] \\ &+ \log\left[\frac{1+\exp\{-h\nu_j/kT\}}{1-\exp\{-h\nu_{0j}/kT_0\}}\right].\end{aligned}$$

- the index k is the species label (k=O_2)
- the subscript j identifies the individual lines of the molecule.
- $\mathcal{F}_j$ is the complex lineshape function,
- $\mathcal{R}^k$ is the isotopic fraction,
- T is temperature in Kelvins,
- T_0=300 K,
- P is pressure in hPa,
- $\mathcal{I}_j\left(T_0\right)$ is the logarithm of the integrated intensity in nm^2 MHz at T_0,
- ν_{pj} is the pressure-shifted (but not Doppler-shifted) line center frequency in MHz,
- ν_{0j} is the unshifted line frequency, as it appears in the JPL Catalog.
- E''^k_j is the lower-state energy for the jth transition in cm^{-1},
- $Q^k(T_0)$ is the partition function at T_0,
- $Q^k(T)$ is a log-linear interpolation of tabulated partition function values,
- $w_d = 3.58117369 \times 10^{-7}\nu\sqrt{\frac{T}{\mathcal{M}}}$ is the Doppler width,
- $\mathcal{M}$ is the absorber molecular mass,

B. Lineshape

The lineshape that we use for each of the Zeeman components is the Fadeeva function, or complex error function, modified to include line interference. The Fadeeva function is the convolution of a Gaussian thermal Doppler lineshape with a Lorentzian collisional lineshape. It has a simple form,

$$\mathcal{F}(z) = \frac{\imath}{\pi}\int_{-\infty}^{\infty}\frac{e^{-t^2}}{z-t}\,dt$$

for complex z, or

$$\begin{aligned}\mathcal{F}(x+\imath y) =& \frac{1}{\pi}\int_{-\infty}^{\infty} e^{-t^2}\left(\frac{y}{(x-t)^2+y^2}\right.\\ &\left.+\frac{\imath(x-t)}{(x-t)^2+y^2}\right)\,dt\\ =& \mathcal{U}(x,y)+\imath\mathcal{V}(x,y)\,.\end{aligned} \tag{19}$$

The real part of the Fadeeva function, $\mathcal{U}(x,y)$, is the Voigt function.

Terms involving line mixing coefficients, Y, are included to model the first-order effects of interference with the lines of the 60-GHz band [10]. The contribution of these terms is negligible for the pressures where Zeeman-splitting is resolved, but they are included so that this model will merge smoothly with the unpolarized model at high pressures. The same mixing coefficient that is tabulated for the unpolarized case [1] is used for each Zeeman component. Line interference can occur only between Zeeman components of the same Δm, so there is no interference among the Zeeman components of the 118-GHz oxygen line.

The expression that we use for the lineshape, including interference, is

$$\begin{aligned}F(x_j,y_j) =& \frac{1}{\pi}\frac{\nu}{\nu_{0j}}\int_{-\infty}^{\infty} e^{-t^2}\left(\frac{y_j - Y_j(x_j-t)}{(x_j-t)^2+y_j^2}\right.\\ &\left.+\frac{\imath(y_jY_j+x_j-t)}{(x_j-t)^2+y_j^2}\right)\,dt\end{aligned} \tag{20}$$

$$= \frac{\nu}{\nu_{0j}}(1+\imath Y_j)\mathcal{F}(x_j+\imath y_j), \tag{21}$$

where

$$\begin{aligned}x_j &= \frac{\sqrt{\ln 2}\left(\nu-\nu_j^k-\Delta\nu_{j,m,\Delta m}\right)}{w_d^k},\\ y_j &= \frac{\sqrt{\ln 2}\,w_{cj}P}{w_d^k}\left(\frac{T_0}{T}\right)^{n_{cj}^k},\\ Y_j &= P\left[\delta_j^k\left(\frac{T_0}{T}\right)^{n_{\delta_j}^k}+\gamma_j^k\left(\frac{T_0}{T}\right)^{n_{\gamma_j}^k}\right],\\ w_d^k &= \sqrt{2\ln 2\,\mathrm{k_B}/c}\sqrt{\frac{T}{\mathcal{M}^k}}\,\nu,\end{aligned}$$

and the line center frequency is shifted according to

$$\nu_j^k = \left[\nu_{0j}^k + \Delta\nu_{0j}^k P\left(\frac{T_0}{T}\right)^{n_{\Delta\nu_{0j}}^k}\right]\left(1+\frac{v_{\text{los}}}{c}\right). \tag{22}$$

Line parameters, which are tabulated in the scalar forward model algorithm description [11]; these include unshifted line center frequency, ν_{0j}, [7] collisional linewidth parameter, w_{cj}^k, collisional linewidth temperature dependence exponent, n_{cj}^k, line pressure shift parameter, $\Delta\nu_{0j}^k$ line pressure shift temperature dependence exponent, $n_{\Delta\nu_{0j}}^k$ and line interference parameters, δ_j^k, $n_{\delta_j}^k$, γ_j^k, $n_{\gamma_j}^k$.

A line pressure shift, $\Delta\nu_{0j}^k = -0.14$ MHz/hPa, [12] was used in the initial version of software, but radiance residuals of retrievals using MLS band 1 (a 25-channel filterbank centered on the 118-GHz O_2 line) show a pressure-shift-like residual consistent with a shift of nearly this magnitude, but of opposite sign. Laboratory measurements [13] indicate a shift magnitude of less than 0.1 MHz/hPa. The current version (v01.51) of the Level 2 software uses $\Delta\nu_{0j}^k = 0$.

The line-of-sight velocity, v_{los}, due to spacecraft motion, Earth rotation, and wind results in a Doppler shift of all Zeeman components that may be considered constant across the bandwidth of interest. This velocity is considered positive if the observer and atmosphere are moving toward one another.

The Zeeman frequency shifts are

$$\Delta\nu_{J,m,\Delta m} = (m_u/J_u g_u - m_l/J_l g_l)\mathcal{B}_{\text{geo}}\,, \tag{23}$$

where g values for the upper and lower states are from the JPL database. For the 118-GHz line, the shifts are

$$\begin{aligned}\Delta\nu_{\sigma+} &= \kappa\mathcal{B}_{\text{geo}}\\ \Delta\nu_{\sigma-} &= -\kappa\mathcal{B}_{\text{geo}}\\ \Delta\nu_{\pi} &= 0\end{aligned} \tag{24}$$

where κ=1.4012 MHz/gauss.

The leading $\frac{\nu}{\nu_{0j}}$, which gives agreement with the Debye non-resonant shape at low frequencies, is nearly constant over the Doppler width and taking it outside of the integral introduces negligible error.

The cross section is summed over all of the lines that contribute significantly. The z_j dependence of the lineshape in [1, Eqn. 30] explicitly includes the absorptive part of the negative-frequency resonance of each line. These terms give the absorption due to the far wing of the emission line at $-\nu_{0j}$, but are neglected here.

V. Geomagnetic Field Model

The geomagnetic field, $\boldsymbol{\mathcal{B}}_{\text{geo}}$, is provided by the International Geomagnetic Reference Field (IGRF) model [14][15], an empirical representation of the Earth's core magnetic field recommended for scientific use by the International Association of Geomagnetism and Aeronomy (IAGA). In the absence of magnetic storms and outside of the auroral belts, we estimate that field variation at the altitudes below 120 km may be on the order of 5 percent, but there is significant uncertainty in this value.

Profiles of IGRF in the Earth centered rotating (ECR) frame are included in the Level 2 state vector. They are interpolated, as needed, to positions along the integration path and rotated to the instrument field of view polarized pointing (IFOVPP) coordinate system. The IFOVPP is defined such that the instrument boresight is in the $-\hat{z}$ direction and receives polarized radiation with Poynting vector in the $\hat{z}$ direction, whose electric field is in the $\hat{x}$ direction, and whose magnetic field is in the $\hat{y}$ direction.

The EOSDIS Science Data Production (SDP) Toolkit [16], provides ECR-to-ECI and ECI-to-Spacecraft rotations, and the EOS MLS Calibration Report [17] includes the transformation from spacecraft coordinates to the field of view of each of the radiometers. The FOV defined in [18], has its $+\hat{z}$ along the antenna boresight and $\hat{x}$ in the direction of the magnetic field vector, so this frame of reference may be transformed to IFOVPP by $\hat{z} \rightarrow -\hat{z}$, $\hat{x} \rightarrow \hat{y}$, $\hat{y} \rightarrow \hat{x}$. The R1B antenna polarization is almost exactly orthogonal to that of the R1A antenna and the antennas are nearly co-aligned, so calculated R1B radiances on the pointing grid (before frequency and spatial convolution) are the cross-polarization of the R1A calculation.

ECR-to-IFOVPP rotation matrices are provided for each minor-frame integration (MIF), for the polarization and pointing of the central axis of the R1A antenna at the middle of each integration. These matrices are required to transform geomagnetic field into the frame in which radiative transfer calculations are performed. However, the radiative transfer calculations are actually done on a uniform pointing grid and then convolved with the antenna pattern to give MIF-modeled radiances. We need ECR-to-IFOVPP, not for the MIF pointings, but on the forward model pointing grid. Rather than interpolate (and extrapolate) the rotation matrices from the MIF grid to the radiative transfer pointing grid, we use the rotation matrix from the closest MIF. Pointings in the radiative transfer grid that have higher tangent points than that of the highest tangent-point MIF center all use the rotation matrix from the highest MIF. Errors introduced should be small compared to those from other sources of uncertainty in the magnetic field.

VI. Derivatives

A. General Form of Polarized Derivatives

The equation of polarized radiative transfer, (10), may be differentiated with respect to a state vector element, x, to give the derivatives required by retrievals. As always, care must be taken in the tensor case to preserve matrix order. In the following expressions, we do not explicitly show the break in indexing at the tangent point.

$$\begin{aligned} \frac{\partial \boldsymbol{I}(x)}{\partial x} &= \frac{\partial}{\partial x} \sum_{i=1}^{2N} \boldsymbol{\mathcal{T}}_i \, \Delta B_i \\ &= \sum_{i=1}^{2N} \frac{\partial \boldsymbol{\mathcal{T}}_i}{\partial x} \, \Delta B_i + \boldsymbol{\mathcal{T}}_i \, \frac{\partial \Delta B_i}{\partial x} \end{aligned} \tag{25}$$

The derivative of $\boldsymbol{\mathcal{T}}_i$ may be built up, for successive layers, by differentiating the recurrence relation, $\boldsymbol{P}_i = \boldsymbol{P}_{i-1}\boldsymbol{E}_{i-1}$.

$$\frac{\partial \boldsymbol{P}_i}{\partial x} = \frac{\partial \boldsymbol{P}_{i-1}}{\partial x}\boldsymbol{E}_{i-1} + \boldsymbol{P}_{i-1}\frac{\partial \boldsymbol{E}_{i-1}}{\partial x} \tag{26}$$

with

$$\frac{\partial \boldsymbol{\mathcal{T}}_i}{\partial x} = \frac{\partial \boldsymbol{P}_i}{\partial x}\boldsymbol{P}_i^{\dagger} + \left(\frac{\partial \boldsymbol{P}_i}{\partial x}\boldsymbol{P}_i^{\dagger}\right)^{\dagger}. \tag{27}$$

B. Mixing Ratio Derivatives

Mixing ratio coefficients are f^k_{lmn} where k refers to the species, l is vertical coordinate (ζ), m is horizontal coordinate (ϕ) and n is frequency (ν). Frequency is included for the case of EXTINCTION (see [1]), which may be treated as a frequency-dependent species. The expression for incremental opacity (16) is a sum of terms linear in mixing ratio, so the derivatives themselves are trivially expressed by dropping f^k and the summation over species k.

$$\begin{aligned} \frac{\partial \boldsymbol{\Delta\delta}^k_{i\rightarrow i-1}}{\partial f^k_{lmn}} = &\sum_{\Delta m=-1}^{+1} \boldsymbol{\rho}_{\Delta M}(\theta,\phi) \\ &\times \int_{\zeta_i}^{\zeta_{i-1}} \beta^k_{\Delta m}(\zeta,\nu,T,\boldsymbol{\mathcal{B}}_{\text{geo}}) \frac{\mathrm{d}s}{\mathrm{d}h}\frac{\mathrm{d}h}{\mathrm{d}\zeta}\,\mathrm{d}\zeta\,. \end{aligned} \tag{28}$$

The term in (25) involving $\frac{\partial \Delta B_k}{\partial x}$ is zero for mixing ratio derivatives because ΔB_k depends only upon temperature.

The volume mixing ratio (VMR) of $^{16}O_2$ is not retrieved. In the thermosphere, where O_2 VMR begins to drop significantly, O_2 lines are Doppler broadened and there is not enough information to separate temperature from mixing ratio. We currently use the same *a priori* O_2 profile as was used with UARS MLS, which is piecewise-linear in $\zeta \equiv -\log_{10}(P/1\,\text{hPa})$. The break-points of this profile are given in Table II. Its adequacy is a research topic.

TABLE II
a priori O_2 VMR PROFILE LINEAR BREAK-POINTS

ζ	O_2 VMR	approx. height
surface	0.2095	0 km
2.10	0.2095	82 km
2.78	0.2080	91 km
3.52	0.2032	100 km
4.18	0.1447	110 km

C. Temperature Derivatives

Temperature derivatives are complicated in that atmospheric absorption, the source function and the path length (through the hydrostatic model) all depend upon temperature. Fortunately, most of this complexity is identical to that of the unpolarized case. In the polarized expressions, β for each Δm multiplies an appropriate tensor, $\boldsymbol{\rho}$, and is summed over Δm. Temperature coefficients, with respect to which we want to differentiate, are f_{lm}^T where l is vertical coordinate (ζ) and m is horizontal coordinate (ϕ).

As in the unpolarized case, a simplified incremental opacity is used that neglects the temperature dependence in refraction and uses a simplified $\frac{dh}{d\zeta}$. The frequency representation basis is dropped since temperature has no frequency dependence. The simplified incremental opacity has the form

$$\begin{aligned}\Delta\delta_{i\to i-1}^k =& \frac{\Delta s_{i\to i-1}^{\text{refr}}}{\Delta s_{i\to i-1}} \sum_{\Delta m=-1}^{+1} \boldsymbol{\rho}_{\Delta m}(\theta,\phi) \\ &\times \int_{\zeta_i}^{\zeta_{i-1}} \mathsf{f}^k\left(\zeta,\phi\left(\zeta\right),\nu\right) \beta_{j,\Delta m}^k\left(\zeta,\nu,T,\boldsymbol{\mathcal{B}}_{\text{geo}}\right) \\ &\times \frac{H^3}{\sqrt{H^2-H_t^2}} \frac{Tk\ln 10}{g_o R_o^2 \mathcal{M}}\,\mathrm{d}\zeta\,. \end{aligned} \tag{29}$$

Differentiating with respect to temperature gives

$$\begin{aligned}\frac{\mathrm{d}\Delta\delta_{i\to i-1}^k}{\mathrm{d}f_{lm}^T} =& \frac{\Delta s_{i\to i-1}^{\text{refr}}}{\Delta s_{i\to i-1}} \sum_{\Delta m=-1}^{+1} \boldsymbol{\rho}_{\Delta m}(\theta,\phi) \\ &\times \int_{\zeta_i}^{\zeta_{i-1}} \Bigg\{ \mathsf{f}^k \frac{\mathrm{d}\beta_{j,\Delta m}^k(\zeta)}{\mathrm{df}_{lm}^T} \eta_l^T\left(\zeta\right) \eta_m^T\left(\phi\left(\zeta\right)\right) \frac{\mathrm{d}s}{\mathrm{d}h}\frac{\mathrm{d}h}{\mathrm{d}\zeta} \\ &+ \mathsf{f}^k \beta_{j,\Delta m}^k(\zeta) \frac{2H^2\frac{\mathrm{d}H}{\mathrm{d}f_{lm}^T} - 3H_t^2\frac{\mathrm{d}H}{\mathrm{d}f_{lm}^T} + HH_t\frac{\mathrm{d}H_t}{\mathrm{d}f_{lm}^T}}{\left(H^2-H_t^2\right)^{\frac{3}{2}}} \frac{\mathrm{d}h}{\mathrm{d}\zeta} \\ &+ \mathsf{f}^k \beta_{j,\Delta m}^k(\zeta) \frac{\eta_l^T\left(\zeta\right)\eta_m^T\left(\phi\left(\zeta\right)\right)}{T} \frac{\mathrm{d}s}{\mathrm{d}h}\frac{\mathrm{d}h}{\mathrm{d}\zeta} \Bigg\} \mathrm{d}\zeta\,. \end{aligned} \tag{30}$$

Apart from the summation over Δm and the $\boldsymbol{\rho}$ matrices, this expression is identical to the unpolarized case [1, Eqn. 55] except that here we have both the real and imaginary parts of the lineshape in the temperature derivative of β. The derivative of the lineshape, (20), is

$$\begin{aligned}\frac{\mathrm{d}F(x_j,y_j)}{\mathrm{d}T} =& \frac{\nu}{\nu_{0j}}\Bigg[\left(1+\imath Y_j\right)\frac{\mathrm{d}\mathcal{U}}{\mathrm{d}x}\frac{\mathrm{d}x}{\mathrm{d}T} \\ &+ \left(1+\imath Y_j\right)\frac{\mathrm{d}\mathcal{U}}{\mathrm{d}y}\frac{\mathrm{d}y}{\mathrm{d}T} \\ &+ \imath\frac{\mathrm{d}Y}{\mathrm{d}T}\mathcal{U} + \imath\left(1+\imath Y_j\right)\frac{\mathrm{d}\mathcal{V}}{\mathrm{d}x}\frac{\mathrm{d}x}{\mathrm{d}T} \\ &+ \imath\left(1+\imath Y_j\right)\frac{\mathrm{d}\mathcal{V}}{\mathrm{d}y}\frac{\mathrm{d}y}{\mathrm{d}T} - \frac{\mathrm{d}Y}{\mathrm{d}T}\mathcal{V}\Bigg]. \end{aligned} \tag{31}$$

The derivatives of the real and imaginary parts of the Fadeeva function are

$$\begin{aligned}\frac{\partial\mathcal{U}}{\partial y} &= \frac{\partial\mathcal{V}}{\partial x} = 2y\mathcal{V} - 2x\mathcal{U}, \\ \frac{\partial\mathcal{U}}{\partial x} &= -\frac{\partial\mathcal{V}}{\partial y} = 2y\mathcal{V} + 2x\mathcal{U} - 2/\sqrt{\pi}. \end{aligned} \tag{32}$$

From the unpolarized ATBD[11, Equation 9.8],

$$\begin{aligned}\frac{\mathrm{d}\nu_j^k}{\mathrm{d}T} &= \frac{(\nu_{0j}^k v_c - \nu_j^k) n_{\Delta\nu_{0j}}^k}{T}, \\ \frac{\mathrm{d}x_j^k}{\mathrm{d}T} &= -\frac{x_j^k}{2T} - \frac{\sqrt{\ln 2}\,(\nu_{0j}^k v_c - \nu_j^k) n_{\Delta\nu_{0j}}^k}{T w_d^k}, \\ \frac{\mathrm{d}y_j^k}{\mathrm{d}T} &= -\frac{y_j^k (n_{cj}^k + \frac{1}{2})}{T}, \\ \frac{\mathrm{d}Y_j^k}{\mathrm{d}T} &= -P\left[\frac{n_{\delta_j}^k \delta_j^k}{T}\left(\frac{T_0}{T}\right)^{n_{\delta_j}^k} + \frac{n_{\gamma_j}^k \gamma_j^k}{T}\left(\frac{T_0}{T}\right)^{n_{\gamma_j}^k}\right]. \end{aligned} \tag{33}$$

D. $\boldsymbol{\beta}$ Derivatives

Derivatives of quantities on which $\Delta\delta_{i+1\to i}^k$ has dependence only through β can be written

$$\frac{\partial\boldsymbol{\Delta\delta}_{i\to i-1}^k}{\partial x_j} = \sum_{\Delta m=-1}^{+1} \boldsymbol{\rho}_{\Delta M} \int_{\zeta_i}^{\zeta_{i-1}} f_{lmn}^k \frac{\mathrm{d}\beta_{\Delta m}^k}{\mathrm{d}x_j}\frac{\mathrm{d}s}{\mathrm{d}h}\frac{\mathrm{d}h}{\mathrm{d}\zeta}\,\mathrm{d}\zeta\,. \tag{34}$$

This class includes derivatives with respect to spectroscopic parameters, wind-induced Doppler shifts, and magnetic field.

VII. Field of View Convolution

The method of field-of-view convolution is discussed in [1, Eqn. 64].

$$I\left(\Omega_t\right) = \frac{\mathrm{Tr}\int_{\Omega_A} \boldsymbol{I}\left(\Omega\right)\boldsymbol{G}\left(\Omega-\Omega_t\right)\mathrm{d}\Omega}{\mathrm{Tr}\int_{\Omega_A}\boldsymbol{G}\left(\Omega-\Omega_t\right)\mathrm{d}\Omega}\,, \tag{35}$$

where Ω is the solid angle over which radiative transfer has been calculated, Ω_t is the pointing of the antenna to be modeled and Ω_A is the solid angle over which the polarized, far-field antenna pattern tensor, $\boldsymbol{G}\left(\Omega-\Omega_t\right)$ has been measured. For both R1A and R1B, the cross-polarized antenna patterns are 30 dB or more below the co-polarized patterns [17]. Currently, the cross-polarization is ignored, permitting the use of the same software as is used in the unpolarized case. Resulting errors in calculated brightness are estimated to be less than 0.2 K.

After field-of-view convolution, power is a scalar so the unpolarized, scalar algorithm for frequency averaging may be followed without approximation.

VIII. Polarized L2PC Model

The MLS Level 2 retrieval software [19] requires Jacobians, partial derivatives of the radiances with respect to state vector elements. Unfortunately, the cost of producing polarized derivatives during routine processing is currently prohibitive. To speed processing, radiances and derivatives are precomputed for climatological conditions and tabulated as Level 2 processing coefficient (L2PC) files for use as the linearization point and Jacobian of a fast, linear retrieval.

Polarized L2PCs contain temperature derivatives for DACS bands 22 and 26 calculated on a grid of magnetic field strengths and orientations. In the current version (v1.5) of Level 2 software, the closest bin to the field strength and elevation angle (the angle between the field and the line-of-sight) is used.

Interpolation in azimuth angle, ϕ, is done analytically, since the 2x2 intensity matrix, $\boldsymbol{I}$, or any of its derivatives, may be rotated to give values for any ϕ. Given (9) and (8), we can write

$$\begin{aligned} I_{\parallel}(\phi) = &\cos^2(\phi) I_{\parallel}(0^\circ) + \sin^2(\phi) I_{\perp}(0^\circ) \\ &+ 2\cos(\phi)\sin(\phi) I_{|}(0^\circ)\,. \end{aligned} \tag{36}$$

This expression may be recast in terms of double-angle sines and cosines, and in terms of $I_{\parallel}$ (the [1,1] element of $\boldsymbol{I}$) for three values of ϕ rather than three elements of $\boldsymbol{I}$ for $\phi = 0$.

$$\begin{aligned} I_{\parallel}(\phi) = &\frac{1+\cos(2\phi)-\sin(2\phi)}{2} I_{\parallel}(0^\circ) \\ &+ \frac{1-\cos(2\phi)-\sin(2\phi)}{2} I_{\parallel}(90^\circ) \\ &+ \sin(2\phi) I_{\parallel}(45^\circ)\,. \end{aligned} \tag{37}$$

This formulation is particularly useful because the forward model software is designed to select the parallel ($\|$) component of the radiance or radiance-derivative tensor, and to send arrays of these real, scalar values through the antenna convolution and passband convolution of the host scalar model. The polarized code can be run for $\phi = 0^\circ$, 45° and 90°, and these values may be added as in (37) to produce a model for any ϕ.

In its current configuration, the polarized L2PC model assumes a constant geomagnetic field magnitude and orientation along the integration path. This permits the model to be parameterized by the field value at the tangent point. However, the full forward model (and the real atmosphere) have geomagnetic field variations along the path with resulting radiances that cannot be modeled with a constant field. For example, changes in the field magnitude move the $\sigma_{\pm}$ components in and out, resulting in a broadened spectral feature with weighting functions that depend upon the details of the field along the path. The impact of this approximation upon EOS-MLS retrievals is an area for further research.

IX. Matrix Exponentiation and Derivatives

The exponential of a 2x2 matrix (Sylvester's identity) is

$$\exp(\boldsymbol{A}) = e^{\lambda_2}\left[\frac{e^{2d}-1}{2d}(\boldsymbol{A}-\lambda_2\mathbf{1})+\mathbf{1}\right], \tag{38}$$

where λ_1, λ_2 are eigenvalues of $\boldsymbol{A}$, $d \equiv \frac{1}{2}(\lambda_1 - \lambda_2)$ and $\mathbf{1}$ is the 2×2 identity matrix. This form is well behaved as $d \to 0$. The derivative of a matrix exponential with respect to p is

$$\begin{aligned} \frac{\mathrm{d}\exp(\mathbf{A})}{\mathrm{d}p} = \; & e^s \left\{ \frac{\sinh d}{d}\left[s'\mathbf{A} + \mathbf{A}' + (d'd - s's)\mathbf{I}\right] \right. \\ & \left. + \frac{d\cosh d - \sinh d}{d^2}\left[d'\mathbf{A} + (s'd - d's)\,\mathbf{I}\right] \right\}, \end{aligned} \tag{39}$$

where $s \equiv \frac{1}{2}(\lambda_1 + \lambda_2)$, $d' = \frac{\mathrm{d}d}{\mathrm{d}p}$, $s' = \frac{\mathrm{d}s}{\mathrm{d}p}$, $\boldsymbol{A}' = \frac{\mathrm{d}\boldsymbol{A}}{\mathrm{d}p}$. As the eigenvalues coalesce, no cancellations occur, and no infinities arise if the elements of $\mathbf{A}$ and $\mathbf{A}'$ are finite.

X. Results from early MLS data

Fig. 4 shows simulated, single-frequency, single-ray limb radiances for the centers of the 61 DACS channels that are used in MLS retrievals. Seven limb-pointings are shown, with tangent pressures ranging from 100 hPa to 0.0001 hPa. The six panels are for six orientations of geomagnetic field, $\boldsymbol{\mathcal{B}}_{\text{geo}}$, with inset axes showing the orientation $\boldsymbol{\mathcal{B}}_{\text{geo}}$ with respect to the propagation direction ($\hat{z}$) and the linear polarization mode under consideration. The geomagnetic field magnitude is 0.5 gauss in all cases. Single-frequency, single-pointing simulated radiances such as these are convolved with MLS channel frequency response functions and antenna patterns to produce simulated channel radiances.

In the upper right panel, $\boldsymbol{\mathcal{B}}_{\text{geo}}$ is along $\hat{\boldsymbol{H}}_{\text{RF}}$ and the π line center is saturated at roughly the physical temperature of the lower thermosphere for the 0.001-hPa pointing. Similarly, in the upper center panel, with $\boldsymbol{\mathcal{B}}_{\text{geo}}$ perpendicular to both $\hat{\boldsymbol{H}}_{\text{RF}}$ and the propagation direction, the two σ lines are opaque for the 0.001-hPa pointing.

In the upper left panel, the σ lines are coupled to circularly polarized modes (σ_+ is right, σ_- is left) and the π line is transparent. On the 0.001 hPa tangent pointing, a right-circularly-polarized antenna would see only the $\sigma+$ line, and would be a shifted version of the upper right panel, saturated at something just below 200 K. The MLS linearly polarized antenna sees half of the saturated right-circular and half of the transparent left-circular modes at the $\sigma+$ line center, and appears to saturate for the 0.001-hPa pointing at roughly half of the physical temperature of the lower thermosphere. Not until the 0.1-hPa tangent pointing does the collisionally-broadened wing of the $\sigma-$ line saturate at the $\sigma+$ line center.

Fig. 5 and fig. 6 show comparisons of MLS measurements and the corresponding forward model calculations from a retrieval that uses these radiances. This early version of MLS level-2 retrieval software is not optimized for the mesosphere and lower thermosphere and does not have necessary degree(s) of freedom in the thermospheric temperature profile to fit the saturated line centers. This inadequacy will be addressed in further work. Line placement and general morphology show good agreement between modeled and measured radiances.

References

[1] W. G. Read, Z. Shippony, and W. V. Snyder, "The clear-sky unpolarized forward model for the EOS Aura microwave limb sounder (MLS)," *IEEE Trans. Geosci. Remote Sensing: The EOS Aura mission*, 2005, (this issue).

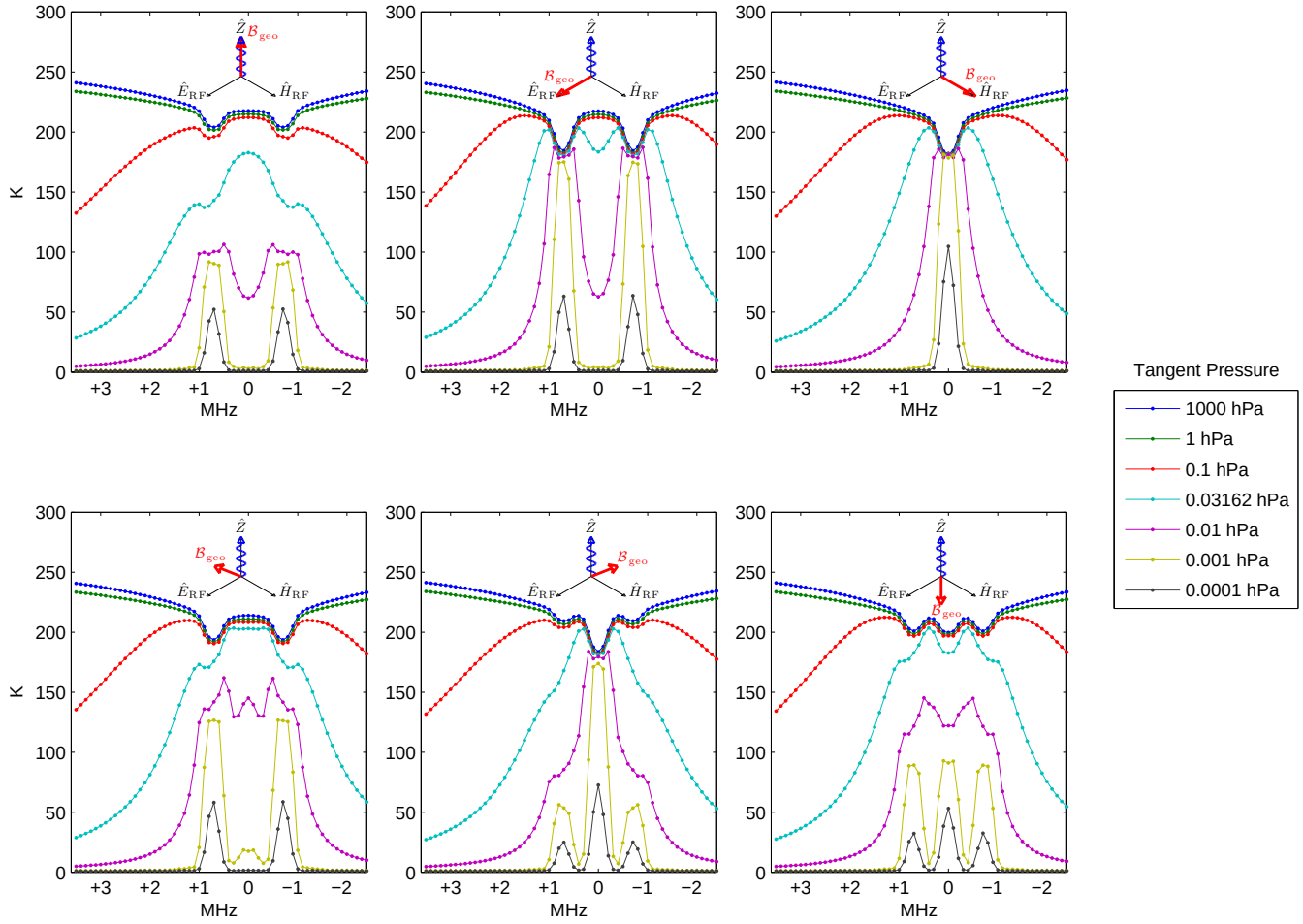

Fig. 4. This figure shows single-frequency, single-ray, simulated limb radiances covering the Zeeman components of the 118-GHz O_2 line. The six panels show simulations for six orientations of geomagnetic field, $\boldsymbol{\mathcal{B}}_{\text{geo}}$, with respect to the polarization and propagation directions of the linear polarization mode under consideration. In all cases, geomagnetic field magnitude is 0.5 gauss. Doppler-broadened cores of the lines are fully saturated at 0.001 hPa. In the top left panel, propagation is along $\boldsymbol{\mathcal{B}}_{\text{geo}}$ and the σ_+ (higher frequency) and σ_- (lower frequency) lines are right and left circularly polarized respectively. Along the 0.001 hPa tangent-pressure ray, the line centers are opaque for one circular mode and transparent for the other and a linear polarization consists of half of each. In the top middle panel, $\boldsymbol{\mathcal{B}}_{\text{geo}}$ is aligned with $\hat{\boldsymbol{E}}_{\text{RF}}$ and the $\sigma_\pm$ lines are linearly co-polarized with the mode under consideration. In the top right panel, $\boldsymbol{\mathcal{B}}_{\text{geo}}$ is aligned with the antenna's $\hat{\boldsymbol{H}}_{\text{RF}}$ direction and the π line is co-polarized with the mode under consideration.

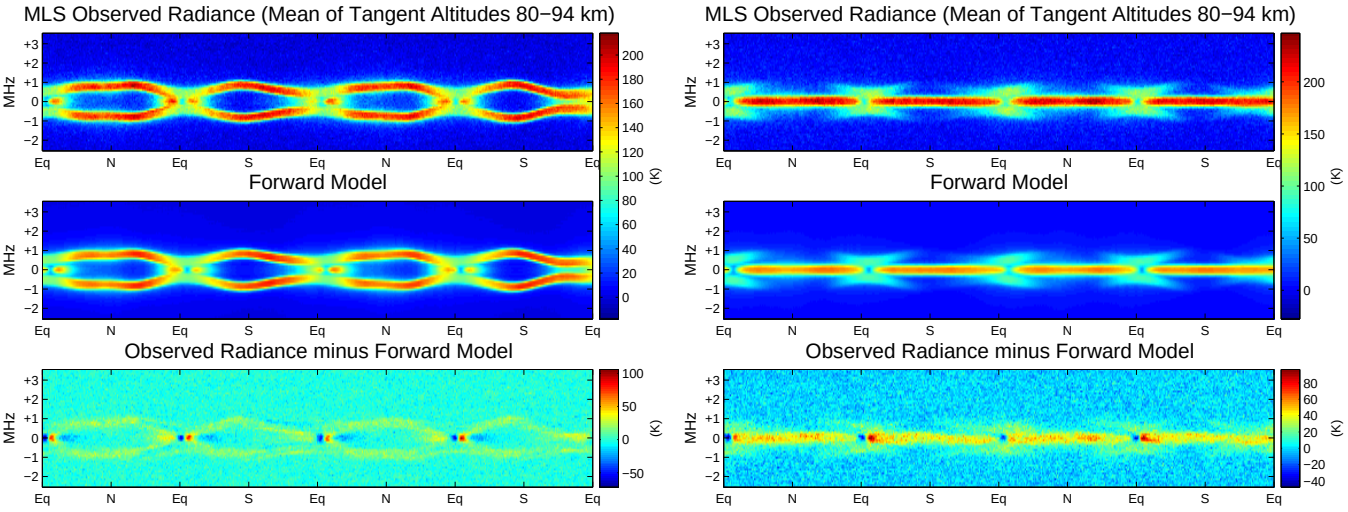

Fig. 5. The top panels show averages of measurements (R1A on left, R1B on right) with tangent points above 80 km, for two orbits from September 1, 2004. The middle panels are simulations of the observations shown in the top panels. They were produced during a level-2 retrieval similar to version v01.51, but with band 26 (R1B DACS) included. At high latitudes, $\boldsymbol{\mathcal{B}}_{\text{geo}}$ is nearly normal to the earth's surface and R1A ($\hat{\boldsymbol{H}}_{\text{RF}}$ horizontal) sees the $\sigma\pm$ lines while R1B ($Hatrf$ vertical) sees the π line. Residuals in the line centers may be due to the limited degrees of freedom in the thermospheric temperature profile in the current Level 2 configuration. Residuals are worse for the pi line, which saturates higher than the σ lines.

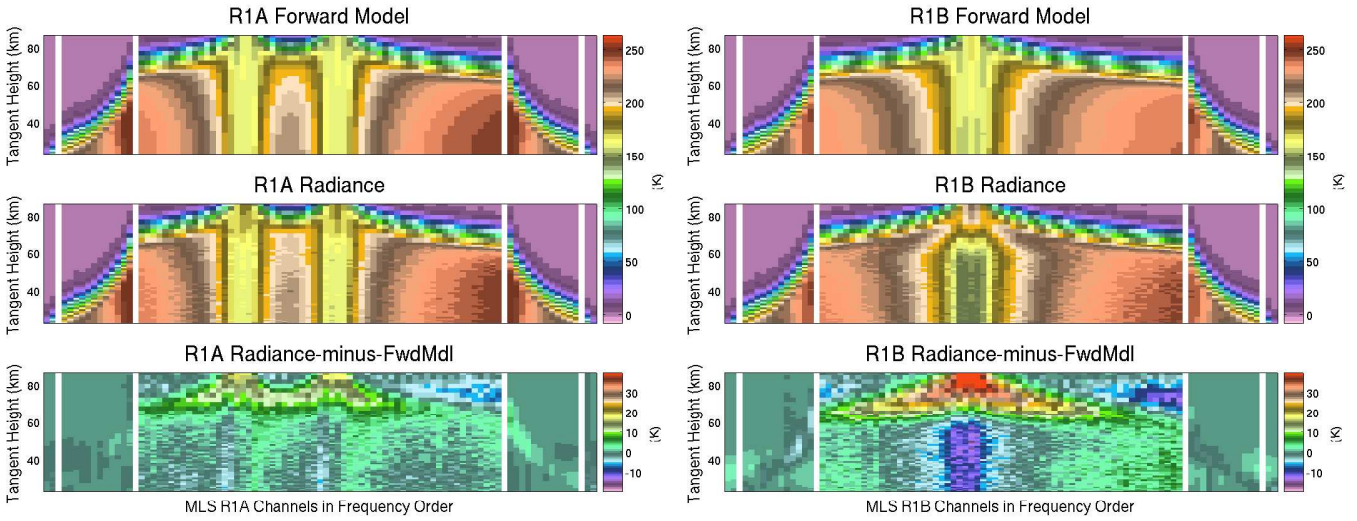

Fig. 6. These figures show R1A (left) and R1B (right) radiances, and the forward model and residuals from a temperature retrieval for data from September 1, 2004, poleward of 70N. Channels are displayed in frequency order. In the center of each panel, 61 DACS channels cover 59 MHz. The intermediate subpanels each contain 12 filterbank channels, which have bandwidths increasing from 8 MHz in the center to 96 MHz at the outside. The narrow strips on the outsides of each panel are each two 500-MHz wide channels, centered 1750 MHz and 3350 MHz from the line center. The $\hat{\boldsymbol{H}}_{\rm RF}$ vector of R1B is close to the direction of the geomagnetic field, $\boldsymbol{\mathcal{B}}_{\rm geo}$, so we see the π line in R1B. We see the two σ lines, linearly polarized, in R1A.

[2] J. W. Waters *et al.*, "The earth observing system microwave limb sounder (EOS MLS) on the aura satellite," *IEEE Trans. Geosci. Remote Sensing: The EOS Aura mission*, 2005, (this issue).

[3] W. B. Lenoir, "Propagation of partially polarized waves in a slightly anisotropic medium," *Journal of Applied Physics*, vol. 38, no. 13, 1967.

[4] ——, "Microwave spectrum of molecular oxygen in the mesosphere," *Journal of Geophysical Research*, vol. 73, no. 361, 1968.

[5] P. W. Rosenkranz and D. H. Staelin, "Polarized thermal microwave emission from oxygen in the mesosphere," *Radio Science*, vol. 23, no. 5, pp. 721–729, September–October 1988.

[6] A. Stogryn, "The magnetic field dependence of brightness temperatures at frequencies near the O_2 microwave absorption lines," *IEEE Transactions on Geoscience and Remote Sensing*, vol. 27, no. 3, pp. 279–289, May 1989.

[7] H. M. Pickett, R. L. Poynter, E. A. Cohen, M. L. Delitsky, J. C. Pearson, and H. S. P. Muller, "Submillimeter, millimeter, and microwave spectral line catalog," *J. Quant. Spectrosc. Radiat. Transfer*, vol. 60, no. 5, pp. 883–890, 1998. [Online]. Available: see http://spec.jpl.nasa.gov/

[8] C. H. Townes and A. L. Schawlow, *Microwave Spectroscopy*. New York: Dover Publications, Inc., 1955.

[9] M. J. Schwartz, W. V. Snyder, and W. G. Read, "EOS MLS mesosphere-specific forward model algorithm theoretical basis document," Jet Propulsion Laboratory, Pasadena, CA, Mesosphere Specific ATBD JPL D-28534, 4 June 2004, version 1.0. [Online]. Available: http://mls.jpl.nasa.gov

[10] P. W. Rosenkranz, "Shape of the 5 mm oxygen band in the atmosphere," *IEEE Transaction on Antennas and Propagation*, vol. AP-23, no. 4, pp. 498–506, July 1975.

[11] W. G. Read and Z. Shippony, "EOS MLS forward model algorithm theoretical basis document," Jet Propul. Lab., Pasadena, CA, Tech. Rep. JPL D-18130, March 30 2004. [Online]. Available: http://mls.jpl.nasa.gov

[12] M. Y. Tretyakov, V. V. Parshin, V. N. Shanin, S. E. Myasnikova, M. A. Koshelev, and A. F. Krupnov, "Real atmosphere laboratory mesurements of the 118 GHz oxygen line: Shape, shift and broadening of the line," *J. Mol. Spectrosc.*, vol. 208, no. 1, pp. 110–112, 2001.

[13] B. J. Drouin, 2004, personal Communication.

[14] C. E. Barton, "International geomagnetic reference field: The seventh generation," *J. Geomag. Geoelectr.*, no. 49, pp. 123 – 148, 1997.

[15] e. a. M. Mandea. (2000, 26 May) International Geomagnetic Reference Field - epoch 2000 revision of the IGRF for 2000 - 2005. [Online]. Available: http://www.ngdc.noaa.gov/IAGA/wg8/igrf.html

[16] "Version 2.0 SDP toolkit users guide for the ECS project," Raytheon Systems Company, Upper Marlboro, MD, Tech. Rep. 333-CD-100-102, January 1999, prepared under contract NAS5-60000, CDRL item 062.

[17] R. F. Jarnot, R. E. Cofield, H. M. Picket, and P. C. Stek, "EOS MLS instrument calibration report," Jet Propul. Lab., Pasadena, CA, Tech. Rep. JPL D-26280, March 30 2004.

[18] R. E. Cofield *et al.*, "GHz optics design and performance," *IEEE Trans. Geosci. Remote Sensing: The EOS Aura mission*, 2005, (this issue).

[19] N. J. Livesey and W. V. Snyder, "Retrieval algorithms for the EOS Microwave Limb Sounder (MLS) instrument," *IEEE Trans. Geosci. Remote Sensing: The EOS Aura mission*, 2005, (this issue).

Michael J. Schwartz began his undergraduate education at Deep Springs College, received his B.A. in Physics from Carleton College in 1985 and his Ph. D. in Physics from Massachusetts Institute of Technology in 1998. His thesis, supervised by Prof. D.H. Staelin, involved atmospheric remote sensing with millimeter-wave oxygen lines. He was on the research staff of the MIT Research Laboratory of Electronics in 1999, where he contributed to the development of an aircraft-based atmospheric sounding package. In 2000, he joined the Microwave Limb Sounding group at the Jet Propulsion Laboratory. His responsibilities have included the development of digital autocorrelator spectrometer hardware and processing algorithms for the EOS-MLS instrument, oversight of the MLS temperature and geopotential height data products, and development of the polarized forward model for Zeeman-split oxygen lines.